

# Band Gap Extraction from Individual Two-Dimensional Perovskite Nanosheets Using Valence Electron Energy Loss Spectroscopy

Kulpreet S. Viridi,<sup>†</sup> Yaron Kauffmann,<sup>‡</sup> Christian Ziegler,<sup>†,§</sup> Pirmin Ganter,<sup>†,§</sup> Peter Blaha,<sup>||</sup> Bettina V. Lotsch,<sup>†,§</sup> Wayne D. Kaplan,<sup>‡</sup> and Christina Scheu<sup>\*,†,⊥</sup>

<sup>†</sup>Department of Chemistry and Center for NanoScience (CeNS), Ludwig-Maximilians-Universität München, Butenandtstraße 5-13, 81377 Munich, Germany

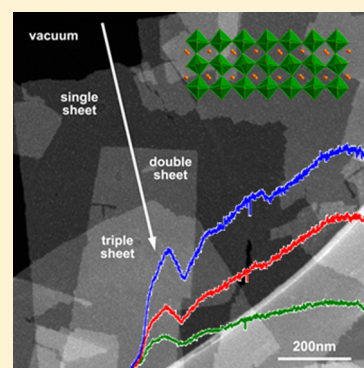
<sup>‡</sup>Department of Materials Science and Engineering, Technion – Israel Institute of Technology, Haifa 32000, Israel

<sup>§</sup>Max Planck Institute for Solid State Research, Heisenbergstraße 1, 70569 Stuttgart, Germany

<sup>||</sup>Institute of Materials Chemistry, Vienna University of Technology, Getreidemarkt 9/165-TC, A-1060 Vienna, Austria

<sup>⊥</sup>Max-Planck-Institut für Eisenforschung GmbH, Max-Planck-Straße 1, 40237 Düsseldorf, Germany

**ABSTRACT:** Rapid progress in the synthesis of nanostructures with tailor-made morphologies necessitates adequate analytical tools to unravel their physical properties. In our study, we investigate, on the nanometer scale, the band gap of individual  $[\text{TBA}_x\text{H}_{1-x}]^+[\text{Ca}_2\text{Nb}_3\text{O}_{10}]^-$  nanosheets obtained through intercalation–exfoliation of the layered bulk phase  $\text{KCa}_2\text{Nb}_3\text{O}_{10}$  with tetra-*n*-butylammonium hydroxide (TBAOH) using valence electron energy loss spectroscopy (VEELS) in the scanning transmission electron microscope (STEM). The nanosheets consist of an anionically charged perovskite layer with cationic organic ligands surrounding it. Because of the hybrid nature, a careful acquisition and analysis protocol is required since the nanosheets disintegrate easily under electron beam irradiation. The VEELS data reveal a fundamental band gap of an individual freely suspended perovskite nanosheet to be  $2.9 \pm 0.2$  eV and optically allowed transitions above  $3.8 \pm 0.2$  eV (optical band gap). The spatial resolution of the measurements is about 9 nm, taking into account 50% of the excitations when illuminating with an incident electron beam of 1 nm diameter. Our investigations reveal that the band gap of an individual nanosheet is not changed significantly compared to the bulk phase, which is confirmed by UV–vis data. This is rationalized by the quasi-2D electronic structure of the bulk material being preserved upon delamination.



## INTRODUCTION

Since the discovery of graphene<sup>1</sup> the scientific community has paid considerable attention to apply the principles of two-dimensional (2D) synthesis to other families of materials. A viable approach to various classes of inorganic 2D-nanostructures has been the solution-mediated delamination of layered bulk materials down to the single sheet level. This has led to the synthesis of 2D-nanosheets based on e.g. oxides,<sup>2</sup> boron nitride,<sup>3</sup> metal dichalcogenides,<sup>4</sup> and metal disulfides.<sup>5</sup> One prominent class of such materials is derived from the Dion–Jacobson family of layered perovskites, with the prototypic member  $\text{KCa}_2\text{Nb}_3\text{O}_{10}$ .<sup>6,7</sup> This perovskite was delaminated into 2D-nanostructures consisting of monolayer sheets for the first time about two decades ago.<sup>8</sup> A systematic study of the synthesis procedure and corresponding characterization of the sheets was made by Schaak and Mallouk.<sup>9</sup>  $[\text{TBA}_x\text{H}_{1-x}]^+[\text{Ca}_2\text{Nb}_3\text{O}_{10}]^-$  nanosheets have a structure similar to the layered Dion–Jacobson perovskite  $\text{KCa}_2\text{Nb}_3\text{O}_{10}$  shown in Figure 1a. The  $\text{K}^+$  ions of  $\text{KCa}_2\text{Nb}_3\text{O}_{10}$  are chemically replaced during the intercalation process by the bulky tetra-*n*-butylammonium cations. This replacement is accompanied by the introduction of a large amount of water and causes a significant reduction in the interaction between adjacent

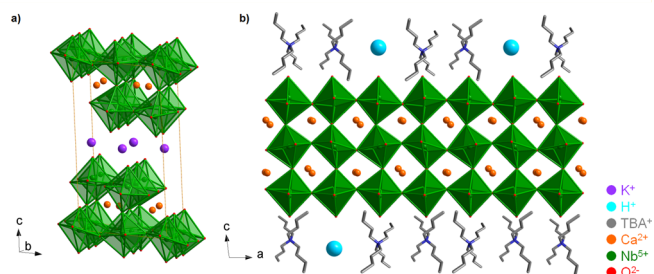


**Figure 1.**  $\text{KCa}_2\text{Nb}_3\text{O}_{10}$  has a layered structure (a) with parallel planes of  $\text{K}^+$  ions sandwiched between perovskite blocks consisting of corner-sharing  $\text{NbO}_6$  octahedra (illustrated in green with red oxygen atoms at the apex and Nb atoms in the center), filled with  $\text{Ca}^{2+}$  ions on the A site positions.  $[\text{TBA}_x\text{H}_{1-x}]^+[\text{Ca}_2\text{Nb}_3\text{O}_{10}]^-$  nanosheets (b) have a structure derived from  $\text{KCa}_2\text{Nb}_3\text{O}_{10}$  where the  $\text{K}^+$  ions are replaced by bulky  $\text{TBA}^+$  and protons for charge balance.

$[\text{Ca}_2\text{Nb}_3\text{O}_{10}]^-$  perovskite blocks to the extent that the blocks become independent of each other. In contrast to the structure

Received: January 6, 2016

Revised: April 30, 2016

Published: May 2, 2016

of other types of nanosheets<sup>3</sup> such as BN or MoS<sub>2</sub> where the delaminated structure is charge neutral, [TBA<sub>x</sub>H<sub>1-x</sub>]<sup>+</sup>[Ca<sub>2</sub>Nb<sub>3</sub>O<sub>10</sub>]<sup>-</sup> nanosheets have a “two-component” structure with the delaminated sheet consisting of a [Ca<sub>2</sub>Nb<sub>3</sub>O<sub>10</sub>]<sup>-</sup> block with a layer of charge compensating cationic ligands around it (Figure 1b). These nanosheets have been suggested as possible candidates for various types of applications.<sup>2,9–18</sup> Sasaki and co-workers proposed the use of them as ultrathin dielectrics.<sup>2,10,13,16–18</sup> The group of Osterloh has demonstrated the photochemical water splitting capability of [TBA<sub>x</sub>H<sub>1-x</sub>]<sup>+</sup>[Ca<sub>2</sub>Nb<sub>3</sub>O<sub>10</sub>]<sup>-</sup> nanosheets<sup>11</sup> and investigated the redoxactive sites by photolabeling.<sup>19</sup> They also showed that high angle annular dark field–scanning transmission electron microscopy (HAADF-STEM) is an excellent tool for characterizing the nanosheets loaded with metal and metal oxide nanoparticles.<sup>19</sup> In addition, they used the sheets as an electron transport layer in solution-processed multijunction polymer solar cells.<sup>14</sup> The group of Ishihara showed a high photocatalytic activity of Rh-doped calcium niobate nanosheets for H<sub>2</sub> production from the water/methanol system without catalyst loading,<sup>12</sup> while a cocatalyst was necessary for their N-doped nanosheets which also exhibited excellent photocatalytic properties.<sup>20</sup> In other research studies, several functional multilayers and superlattices were constructed by sequential deposition of [TBA<sub>x</sub>H<sub>1-x</sub>]<sup>+</sup>[Ca<sub>2</sub>Nb<sub>3</sub>O<sub>10</sub>]<sup>-</sup> and other nanosheets.<sup>10,15</sup>

In light of such intense research activities, it is important to understand the electronic properties of these nanosheets, the band gap in particular. Compton et al.<sup>11</sup> determined the optical band gap and found a value of 3.53 eV, whereby the exfoliated material was dried and studied by means of diffuse reflectance measurements. Drying of the nanosheets leads to a restacking of the material and thus does not reflect individual nanosheets anymore. Akatsuka et al. investigated<sup>21</sup> the electronic structure of [TBA<sub>x</sub>H<sub>1-x</sub>]<sup>+</sup>[Ca<sub>2</sub>Nb<sub>3</sub>O<sub>10</sub>]<sup>-</sup> nanosheet films (number of layers between 1 and 10) deposited on an indium tin oxide coated glass. They determined an optical band gap of 3.44 eV for the nanosheets using photocurrent measurements upon ultraviolet illumination and assuming an indirect semiconducting character.<sup>21</sup> The obtained optical band gap values were determined macroscopically and found to be larger than the one reported in the literature for the parent bulk KCa<sub>2</sub>Nb<sub>3</sub>O<sub>10</sub> phase of 3.35 eV, which was determined in an early study via diffuse reflectance spectroscopy.<sup>22</sup> Thus, to facilitate a better comparison of the obtained band gap values, it would be beneficial to use a technique that allows for the detection of individual nanosheets and to use the same technique and ideally same equipment for the nanosheet and bulk measurements in order to minimize e.g. systematic calibration artifacts. One of such techniques can be VEELS in STEM.<sup>23,24</sup>

With the development of commercially available monochromators in recent years, VEELS has become an interesting approach for determining band gaps in STEM with a high spatial resolution.<sup>25–31</sup> Gu and co-workers have demonstrated<sup>25</sup> the applicability of this method for bulk Si and GaN thin films. Erni and Browning<sup>28</sup> successfully used the technique to determine the size-dependent band gap of CdSe quantum dots. Park et al.<sup>26</sup> and Dennenwaldt et al.<sup>30</sup> measured the band gap of amorphous SiO<sub>2</sub> thin films and nanotubes, respectively. Kuykendall et al.<sup>27</sup> applied the technique for measuring the band gaps of individual InGaN nanowires with different atomic ratios while Keller et al. studied Cu(In,Ga)Se<sub>2</sub> thin solar cells.<sup>29</sup> Jiang and Spence investigated ZrSiO<sub>4</sub> and ZrO<sub>2</sub> bulk ceramics

and discussed the effect of surface excitations on band gap values determined by VEELS.<sup>31</sup> In the present work, we demonstrate that we can determine the band gap of beam sensitive [TBA<sub>x</sub>H<sub>1-x</sub>]<sup>+</sup>[Ca<sub>2</sub>Nb<sub>3</sub>O<sub>10</sub>]<sup>-</sup> nanosheets using VEELS, which we shall compare with our findings about bulk KCa<sub>2</sub>Nb<sub>3</sub>O<sub>10</sub>.<sup>32</sup> We describe in detail the acquisition procedure which is necessary to prevent artifacts due to radiation damage. Similar to King et al.,<sup>33</sup> who used optical absorption data to calculate the band gap of bulk In<sub>2</sub>O<sub>3</sub>, we distinguish in the following between the “fundamental gap” (which is the energy position where the first transition occurs) and the “optical gap” (where a significant intensity is measured in the VEELS or the UV–vis data). The results obtained by VEELS are discussed in light of the band structure and compared to the results of UV–vis measurements performed on a macroscopic scale. An important finding is that for our calcium niobate perovskite the fundamental as well as optical band gap values are not changed significantly when going from the 3D to the 2D structure.

## ■ EXPERIMENTAL SECTION

### Synthesis of [TBA<sub>x</sub>H<sub>1-x</sub>]<sup>+</sup>[Ca<sub>2</sub>Nb<sub>3</sub>O<sub>10</sub>]<sup>-</sup> Nanosheets.

The parent bulk material KCa<sub>2</sub>Nb<sub>3</sub>O<sub>10</sub> was synthesized in a method similar to that proposed by Jacobson and co-workers<sup>7</sup> whereby a stoichiometric mixture of commercially available K<sub>2</sub>CO<sub>3</sub> (Merck, >99% purity), CaCO<sub>3</sub> (Grüssing GmbH Germany, 99% purity), and Nb<sub>2</sub>O<sub>5</sub> (Alfa Aesar, 99.5% purity) with a 10% molar excess of K<sub>2</sub>CO<sub>3</sub> was thoroughly ground, mixed, and fired to a temperature of 1200 °C for 60 h. KCa<sub>2</sub>Nb<sub>3</sub>O<sub>10</sub> has a layered structure, as shown in Figure 1a, containing layers of K and Ca atoms along with layers of edge-sharing NbO<sub>6</sub> octahedra. For nanosheet synthesis a methodology similar to that proposed by Ebina et al. was used.<sup>18</sup> KCa<sub>2</sub>Nb<sub>3</sub>O<sub>10</sub> (1 g) was treated with 5 M HNO<sub>3</sub> (40 cm<sup>3</sup>) for 4 days with daily renewal of the acid for conversion to the protonic oxide HCa<sub>2</sub>Nb<sub>3</sub>O<sub>10</sub>·1.5H<sub>2</sub>O. The product was recovered by filtration, washed with water, and air-dried. For exfoliation into nanosheets HCa<sub>2</sub>Nb<sub>3</sub>O<sub>10</sub>·1.5H<sub>2</sub>O (0.2 g) was dispersed in 50 cm<sup>3</sup> TBAOH·30-hydrate (Sigma-Aldrich, 98% purity) aqueous solution at a molar ratio of 1:1. The solution was shaken for 4 weeks and nondispersed solid removed via centrifugation at 3000 rpm.

### Inductive Coupled Plasma–Atomic Emission Spectroscopy and Atomic Force Microscopy.

The chemical composition was measured by inductive coupled plasma–atomic emission spectroscopy (ICP-AES) and revealed a value of  $x \approx 0.8$  for [TBA<sub>x</sub>H<sub>1-x</sub>]<sup>+</sup>[Ca<sub>2</sub>Nb<sub>3</sub>O<sub>10</sub>]<sup>-</sup>.<sup>15</sup> Atomic force microscopy (AFM) measurements were performed on the diluted suspension of nanosheets allowed to dry on a silicon substrate using an Asylum MFP-3D Stand Alone AFM microscope (Asylum Research, Santa Barbara, CA). A Si microcantilever (300 Hz resonant frequency and 26.1 N/m spring constant) was used, and images were taken in tapping mode.

### Transmission Electron Microscopy and Valence Electron Energy Loss Spectroscopy.

For TEM studies the resulting colloidal suspension was diluted 4 times with water and drop-coated onto lacey carbon-coated Cu grids. TEM investigations were performed using a FEI TITAN 80-300 S/TEM equipped with a field emission gun, a Wien-type monochromator, and Gatan Tridiem 866 energy filter having a 2k × 2k CCD camera. The instrument was operated at 300 kV to obtain a high spatial resolution and to minimize beam damage due to radiolysis which is lower at high voltages.<sup>34</sup> For

all spectroscopy measurements, STEM mode was used with convergence and collection angles of 9.5 mrad each. For VEELS measurements a spectrometer dispersion of 0.02 eV/channel was chosen whereas for the core-loss EELS measurements a dispersion of 0.2 eV/channel was used. The full width at half-maximum (FWHM) for the VEELS measurements was 0.20 eV. In total, 20 sheets have been studied, and data have been acquired at five different positions of each sheet.

To obtain a good signal-to-noise ratio (SNR) in the VEELS data, we followed a 2-fold path reported in the literature.<sup>35</sup> One data set was measured using an energy loss range from  $-5$  to  $+35$  eV such that the spectra contained the complete zero-loss peak (ZLP) and also the plasmon excitation. In total, 75 spectra with an acquisition time of 0.01 s each were acquired within 5 s of irradiation. The spectra were aligned and summed into a single spectrum, and the position of the plasmon peak was determined with an accuracy of  $\pm 0.2$  eV. In the next step, we acquired spectra spanning the energy range  $+1.5$  to  $41$  eV such that they contained the tail of the ZLP on the positive side and also the plasmon excitation. Five spectra acquired in this way within the first 5 s of irradiation (acquisition time 0.64 s each) were summed up to obtain a better SNR. This spectrum was calibrated according to the position of the plasmon peak determined previously. The calibrated spectrum was used for band gap determination. For the fundamental and the optical gap linear fitting procedures were applied and the intersections with the baseline were measured. In case of the optical gap value, we performed a linear fit to the low loss region with a strong intensity increase, while for the fundamental gap the first much weaker intensity increase was used.

**UV-vis Spectroscopy.** The optical band gap values of the sheets and the parent bulk material  $\text{KCa}_2\text{Nb}_3\text{O}_{10}$  were also determined on a macroscopic scale by diffuse reflectance spectroscopy. The spectra were acquired at room temperature with a UV-vis-NIR diffuse reflectance spectrometer (Agilent Technologies, Cary 5000) at a wavelength range of 200–800 nm. Samples were studied as powders using a carrier system with a quartz glass window at the edge of the integrating sphere and using  $\text{BaSO}_4$  as an optical standard. The nanosheets were separated by centrifugation (speed of 20 000 rpm), the supernatant was removed, and the pellet was dried at 100 °C. From the reflectance data  $R$  the Kubelka–Munk remission function  $F(R) = (1 - R)^2/2R$  was calculated for both the nanosheet as well as the bulk.<sup>36,37</sup> For a semiconductor with a direct band gap  $F(R)^2 \sim (E - E_g)$  while for an indirect semiconductor  $F(R)^{0.5} \sim (E - E_g)$ .<sup>38</sup> Our density functional theory (DFT) calculations of the parent bulk material  $\text{KCa}_2\text{Nb}_3\text{O}_{10}$  have revealed direct transitions,<sup>32</sup> and our preliminary DFT results of the sheets indicate that the direct semiconductor character is retained. Thus, Tauc plots were obtained by plotting  $(F(R)h\nu)^2$  versus the photon energy, the linear part of the curve was extrapolated to the baseline, and the optical band gap was extracted from the value of intersection.<sup>39</sup> For the fundamental gap we used also a linear fit to determine the value where  $(F(R)h\nu)^2$  is above the baseline.

## RESULTS AND DISCUSSION

AFM images reveal that the nanosheets are a few hundreds of nanometers to a few microns in lateral dimension, and they tend to stack one above the other when dried on the substrate to form regions of multiple sheets (Figure 2a). AFM height profiles indicated jumps in height of about 3.4 nm between the substrate and the single sheet regions. For subsequent steps,

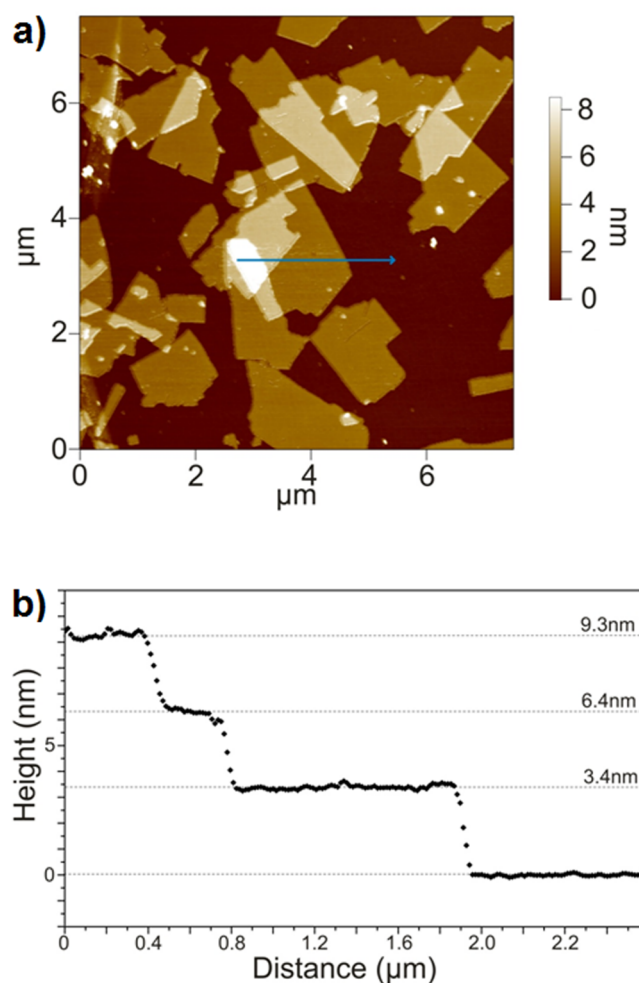


**Figure 2.** AFM image (a) of the  $[\text{TBA}_x\text{H}_{1-x}]^+[\text{Ca}_2\text{Nb}_3\text{O}_{10}]^-$  nanosheets dispersed on a Si wafer, which indicates lateral sizes of the order of a few hundred nanometers. Height profile (b) acquired along the arrow shown in (a) depicts the height of a single nanosheet to be 3.4 nm and that of each subsequent sheet in a stack about 2.9 nm.

however, the increase in height is a little less ( $\sim 2.9$  nm) when one moves from one sheet to the next (Figure 2b). The thickness of the sheets is larger than the values reported in the literature, which range between 1.85 and 3.0 nm as determined by AFM.<sup>19,21,40</sup> Schaak and Mallouk<sup>9</sup> synthesized  $[\text{TBA}_x\text{H}_{1-x}]^+[\text{Ca}_2\text{Nb}_3\text{O}_{10}]^-$  nanosheets and measured a  $[\text{TBA}]^+$  concentration of  $\sim 0.15$ – $0.20$  whereas the  $[\text{TBA}]^+$  concentration in our sheets is higher ( $\sim 0.8$ ), as indicated by ICP-AES data.<sup>15</sup> A height of 1.85 nm was observed by Li et al.<sup>10</sup> using AFM under vacuum conditions. Okamoto et al.<sup>12</sup> synthesized 3% Rh-doped calcium niobate nanosheets (Rh atoms replacing Nb atoms in the nanosheet) and found a height of 2.8–3.0 nm by AFM, which was attributed to adsorption of water and amine on the nanosheet surface.<sup>12</sup> We conclude that the observed higher thickness of our sheets is due to a higher  $[\text{TBA}]^+$  concentration as well as hydration under ambient conditions (AFM measurements were carried out in air and at atmospheric pressure).

HAADF-STEM investigations reveal that the perovskite nanosheets have lateral dimension of a few hundreds of nanometers up to a few microns (Figure 3a), which is in agreement with the AFM measurements. The HAADF-STEM

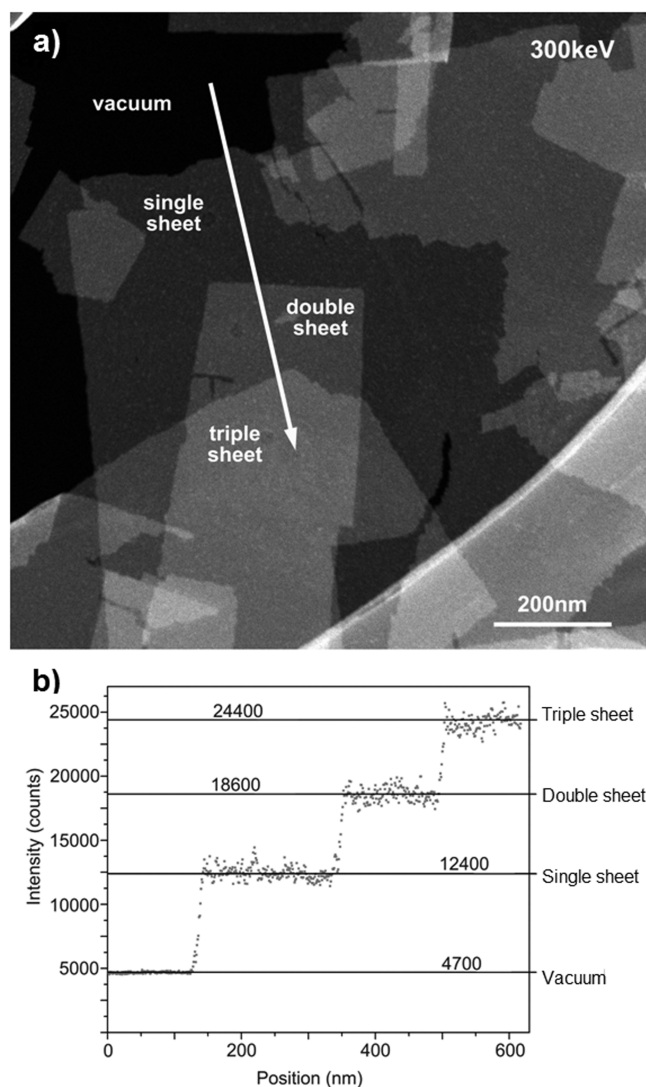


**Figure 3.** HAADF-STEM image (a) shows dark regions representing vacuum and regions with progressively increasing intensity indicating single, double, and triple sheets. The intensity profile (b) along the arrow shown in (a) indicates quantum jumps of intensity when one moves from one sheet to another.

images show dark regions which we classify as vacuum regions (regions without material). This was confirmed by EEL spectra acquired in the dark regions, where the intensity in the low-loss region (1.5–42 eV) was within the noise level indicating absence of any matter. HAADF intensity profiles which are related to mass–thickness contrast<sup>23</sup> show quantum jumps in intensity (Figure 3b), which are attributed to the nanosheets, which are stacked one above the other. Regions where two sheets overlap (labeled double sheets) as well as triple or multiple sheet stacks were observed. The first jump in intensity from vacuum to the region of a single nanosheet (7700 counts) is greater than the following intensity jumps from one sheet to the next sheet (~6000 counts). AFM and STEM-HAADF intensity profiles suggest that the amount and arrangement of TBA<sup>+</sup> ligands differ for the first [Ca<sub>2</sub>Nb<sub>3</sub>O<sub>10</sub>]<sup>-</sup> layer as compared to the situation between two stacked [Ca<sub>2</sub>Nb<sub>3</sub>O<sub>10</sub>]<sup>-</sup> layers. In the latter, parts of the TBA<sup>+</sup> ions may be replaced by H<sup>+</sup> based on the equilibrium reaction  $\text{HCa}_2\text{Nb}_3\text{O}_{10} + \text{TBAOH} \rightleftharpoons \text{TBACa}_2\text{Nb}_3\text{O}_{10} + \text{H}_2\text{O}$  for steric reasons and charge compensation.<sup>41</sup> Hence, a smaller jump in thickness and

intensity in AFM and HAADF is observed in the region where sheets are stacked on top of each other.

The [TBA<sub>x</sub>H<sub>1-x</sub>]<sup>+</sup>[Ca<sub>2</sub>Nb<sub>3</sub>O<sub>10</sub>]<sup>-</sup> nanosheets are highly crystalline as observed by high-resolution transmission electron microscopy (HRTEM). An exemplary HR-TEM image from a single sheet along with its fast Fourier transform (FFT) is shown in Figure 4a. The observed *d*-values of about 3.9 Å

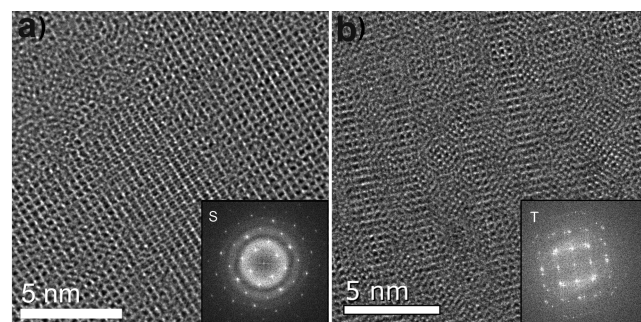


**Figure 4.** HR-TEM images acquired from a single sheet (a) and triple sheets (b) highlight the highly crystalline nature of the sheet as substantiated by the FFTs shown in the insets labeled S for single sheet and T for triple sheets.

match well with the interplanar Nb–Nb distances<sup>42</sup> of 3.93 and 3.86 Å, respectively, in KCa<sub>2</sub>Nb<sub>3</sub>O<sub>10</sub>. In the case of a triple sheet region Moiré fringes appear in the HR-TEM images indicating the presences of three crystalline nanosheets slightly rotated with respect to each other, which is further supported by the corresponding FFT (Figure 4b). This suggests that subsequent nanosheets have negligible interaction between them, which is in agreement with the findings by Akatsuka et al. based on photocurrent measurements of [Ca<sub>2</sub>Nb<sub>3</sub>O<sub>10</sub>]<sup>-</sup> nanosheets.<sup>21</sup>

Core-loss EELS measurements were performed to obtain further insights into the bonding characteristics, oxidation state of the individual atoms and chemical composition of a single nanosheet. The scattering cross section for core-loss excitations is typically several orders of magnitude less than that for the valence loss excitations;<sup>43</sup> hence, to obtain a reasonable signal from a very thin specimen region, a larger acquisition time is required. EEL spectra were acquired in STEM mode cumulatively with an overall acquisition time of 10 s. As will be shown below, in that time frame the sheet structure can decay due to irradiation; however, the measurements still allowed to obtain compositional information, as decomposition induced loss of crystallinity and carbon contamination, but insignificant changes in the elemental ratios. Core-loss EEL spectra of the parent bulk KCa<sub>2</sub>Nb<sub>3</sub>O<sub>10</sub> phase are used for comparison.

The EEL spectrum acquired from a single nanosheet, shown in the top of Figure 5, illustrates the various edges. A comparison with literature allows identifying the edge onsets as follows: 240 eV, Nb-M<sub>4,5</sub> edge;<sup>44,45</sup> 284 eV, C-K edge;<sup>44</sup> 346 eV, Ca-L<sub>2,3</sub> edge;<sup>46</sup> 363 eV, Nb-M<sub>2,3</sub> edge;<sup>45</sup> and 532 eV, O-K edge.<sup>44</sup> The [TBA]<sup>+</sup> ions have a composition of [C<sub>16</sub>H<sub>36</sub>N]<sup>+</sup>, which implies a very low atomic percentage of N in the overall nanosheet structure. Conforming to this, we are hardly able to detect a signal for the N-K edge around 401 eV. The EEL spectrum of bulk KCa<sub>2</sub>Nb<sub>3</sub>O<sub>10</sub> (acquired in diffraction mode) shows the K-L<sub>2,3</sub> edge instead of the C-K edge seen in the nanosheet. This further confirms that during exfoliation nearly

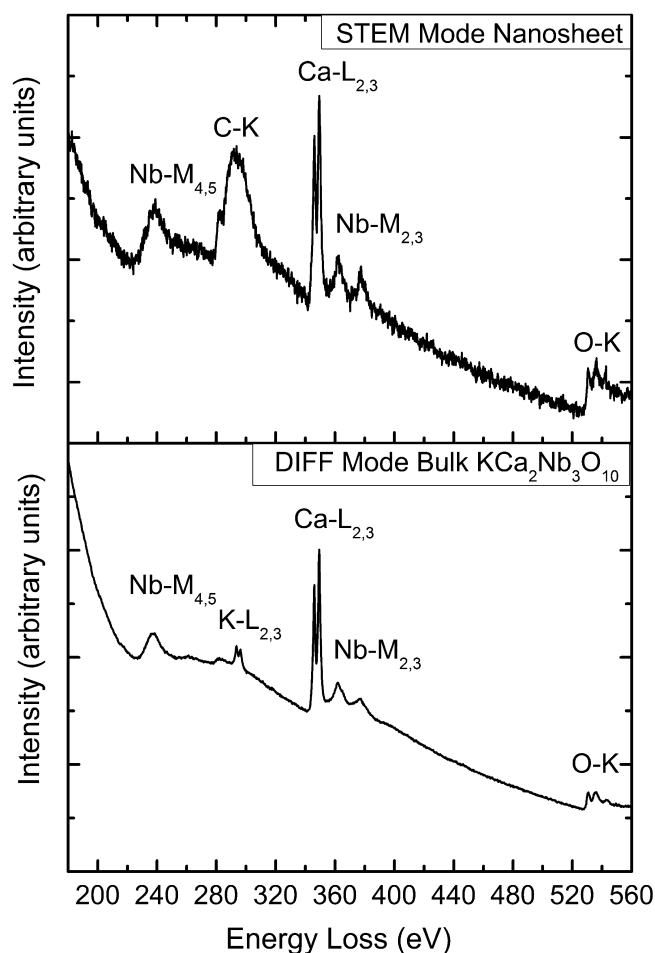


**Figure 5.** Core-loss EEL spectra of  $[\text{TBA}_x\text{H}_{1-x}]^+[\text{Ca}_2\text{Nb}_3\text{O}_{10}]^-$  nanosheets acquired in STEM mode and of bulk  $\text{KCa}_2\text{Nb}_3\text{O}_{10}$  acquired in diffraction mode.

all of the  $\text{K}^+$  ions are replaced by  $[\text{TBA}]^+$  ions, in agreement with the ICP and energy-dispersive X-ray spectroscopy measurements. We did not observe a chemical shift or change in the shape of the energy loss-near edge structure (ELNES) of the element specific ionization edges of the nanosheet compared to the bulk. This indicates that the valence state and type of bonding within the nanosheet remains similar as in the bulk, e.g.,  $\text{Ca}^{2+}$  and  $\text{Nb}^{5+}$ .

To determine the band gap of the nanosheets, it was necessary to identify a single sheet region, which we were able to do by using the STEM-HAADF intensity profile. Second, to obtain high spatial resolution, spectra had to be acquired with a small stationary spot positioned on the nanosheet. However, a hybrid nanostructure when irradiated with 300 kV electrons at a stationary spot of diameter  $<1$  nm could disintegrate. As such, before making a comprehensive set of measurements, understanding the possible degradation of the material under the acquisition conditions is crucial. To this end we acquired 50 spectra at a rate of 1 acquisition per second, irradiating a spot on a single sheet region. The successive VEEL spectra are depicted in Figure 6 and illustrate a change in the state of the sample as it is (carbon) contaminated and damaged due to the electron beam. We found that there is no significant difference between the spectra acquired within the first 5 s; hence, we assumed that there was no apparent damage to the nanosheet in the first 5 s of irradiation. Furthermore, we imaged a single

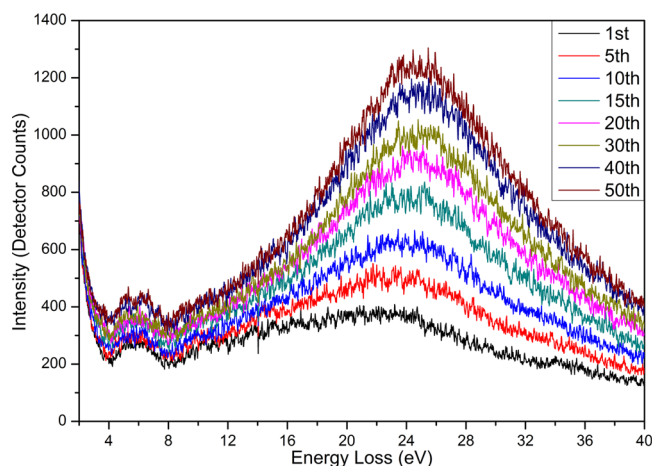


**Figure 6.** Deterioration of the nanosheets with time is exemplified by the change in the VEEL spectra showing the spectra acquired after 1, 5, 10, 15, 20, 30, 40, and 50 s of irradiation under the electron beam.

sheet region after 5 s of irradiation and found no perceivable damage. As such, all VEEL spectra used for analysis were acquired within the first 5 s of irradiation with a stationary electron beam.

Nanostructures by virtue of their small sizes have a very small double differential scattering cross section, and as such the intensity of their valence loss excitations in the VEEL spectrum is very low (Figure 7a). A closer look at the valence loss (inset in Figure 7a) shows that the intensity of the valence loss excitations is 3 orders of magnitude less than that of the ZLP. Consequentially, it was practically impossible with our experimental setup to obtain a better SNR when the ZLP and the valence loss excitations are acquired in the same spectrum. Therefore, we used the 2-fold path<sup>35</sup> as described in detail above. The sum of five spectra acquired with the complete ZLP and the plasmon excitation were used to determine the position of the plasmon peak. The high noise level of the plasmon peak limited the accuracy to  $\pm 0.2$  eV (Figure 7a). A second set of five spectra were acquired containing the tail of the ZLP on the positive side and also the plasmon region, summed up and calibrated according to the position of the plasmon peak from the other data set. The resulting spectrum has a good SNR as illustrated in the Figure 7b and was used for band gap determination for a single sheet region. The process was repeated for acquiring the VEEL spectra from double and triple sheet regions.

The conduction band onset can be determined from a VEEL spectrum upon careful subtraction of the ZLP and by using different deconvolution routines.<sup>25,28,47</sup> Performing a Fourier-log or Fourier-ratio deconvolution of noisy data can introduce artifacts and was thus not applied in the present work. The tails of the ZLP are noisy in our data, and therefore subtracting a spectrum acquired in vacuum as an approximation to the ZLP could be counterproductive. Hence, instead we subtracted the tail of the ZLP by describing it with a power-law function similar to Erni and Browning.<sup>28</sup> The energy loss range for the fit was 1.8–2.5 eV, in accordance with the values which we had used in our previous work to determine the band gap of the bulk  $\text{KCa}_2\text{Nb}_3\text{O}_{10}$  phase.<sup>32</sup> However, we did not use a Lorentzian fit to the first derivative to determine the onset, but rather we determined the fundamental band gap by using a linear fit and measuring the intersection with the baseline of the ZLP-subtracted spectrum. Because of the nanodimensions of

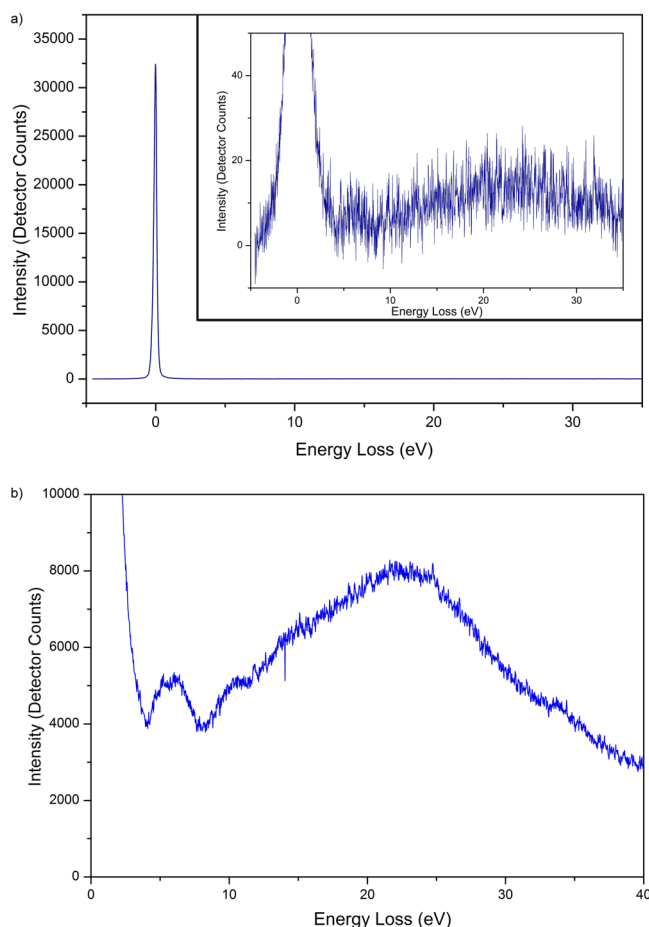


**Figure 7.** VEEL spectrum acquired from a single sheet (a) shows very little signal for valence loss excitations as exemplified by the magnified view in the inset. When a separate spectrum is acquired for the valence excitations alone, a better signal-to-noise ratio can be obtained (b).

the structures investigated, the probability of multiple scattering is negligible; hence, we did not apply any deconvolution routine to the VEEL spectrum.

ZLP-subtracted VEEL spectra from the single, double, and triple sheets are presented in Figure 8a. The fundamental conduction band onset for the single, double, and triple sheet regions is the same and amounts to  $2.9 \pm 0.2$  eV, whereby the error is governed by the alignment procedure described above, i.e., determining the plasmon peak position in the individual noisy spectra. As can be seen in the zoom-in of the spectrum acquired at a single sheet, above the fundamental gap a low intensity region occurs followed by a strong increase in intensity (Figure 8b). The low intensity at the beginning is related to the low density of states in this regime as revealed in our DFT calculation for the bulk phase<sup>32</sup> and in preliminary calculations of the nanosheets. Dipole-forbidden transitions and weak (optical) transition matrix elements are most likely responsible for this low signal, which is also observed for the bulk phase (Figure 8c,d) similar to the results discussed by King et al.<sup>33</sup> for bulk  $\text{In}_2\text{O}_3$ . The fundamental gap for the bulk phase is  $3.2 \pm 0.1$  eV as we have reported previously.<sup>32</sup> Besides the fundamental gap remaining essentially unchanged when going from the 3D structure to the nanosheet, the same holds true for the optical gap determined by VEELS, where we found values of  $3.8 \pm 0.2$  and  $3.9 \pm 0.1$  eV for the nanosheet and the

parent bulk phase  $\text{KCa}_2\text{Nb}_3\text{O}_{10}$ , respectively (see Figure 8). All values are summarized in Table 1.

The fact that the optical and fundamental band gap values are similar for the nanosheets and the bulk is also confirmed by UV–vis diffuse reflectance measurements which are presented in Figure 9a,b. The bandgap values estimated via Tauc plots (using  $(F(R)h\nu)^2$  as a function of the photon energy) yield a fundamental gap value of  $3.4 \pm 0.1$  eV and an optical gap of  $3.6 \pm 0.1$  eV for both the powder of turbostratically restacked nanosheets and the parent bulk phase  $\text{KCa}_2\text{Nb}_3\text{O}_{10}$  (Table 1). A similar discrepancy of around 0.2 eV for the optical gap values determined by VEELS and UV–vis data was observed by Erni and Browning.<sup>28</sup> Most likely this is related to the fact that we did not normalize the absorption coefficient, resulting in an underestimation of band gap values using Tauc plots.<sup>36</sup> In addition, calibration errors of our energy loss dispersion values can explain the difference between the UV–vis and VEELS data. The higher value of the fundamental gap determined by UV–vis diffuse reflectance data might be related to the uncertainties arising from the fact that we do not measure dipole-forbidden transitions in the reflectance data but only those with a weak (optical) transition matrix element.<sup>33</sup>

It is worthwhile comparing our band gap values determined by UV–vis diffuse reflectance spectroscopy to the ones reported in the literature.<sup>11,21,22</sup> Our optical band gap value for the nanosheets are slightly larger than the values of Compton et al.<sup>11</sup> and Akatsu et al.<sup>21</sup> One reason for this is that the determined band gap values depend on the analysis routine and the photon energy region used for doing the linear fit procedure.<sup>33,37,39</sup> Furthermore, we assumed a direct semiconducting character as predicted by our DFT calculation, while Akatsu et al. assumed an indirect semiconductor for the Tauc plot analysis.<sup>21</sup> Besides this, the studied nanosheets might differ slightly in their chemical composition, as the ligand shell around the nanosheets is a mixture of protons and *n*-tetrabutylammonium cations with varying compositions (see above).<sup>11,21</sup> In particular, the different fitting routine and a different experimental setup used by Domen et al. might be responsible for the lower optical band gap value which they found for the bulk phase.<sup>22</sup> Since we applied the same type of spectrometer as well as VEELS on the nanosheet and the bulk material, we are confident to conclude that the band gap is not strongly modified when going from the 3D to the 2D structure.

It is well-known that the valence excitations in VEELS are not localized to specific atoms but span larger regions partly because the valence electrons are delocalized.<sup>48–51</sup> For example, Couillard et al. showed that in nanostructured multilayered gate oxides, despite a small local probe confining to a single layer, the excitations due to interband transitions, interface plasmons, and Cerenkov radiation of the multiple layers interfere, thereby making it hard to extract the signal of a single layer from the stack.<sup>51</sup> In light of the above-mentioned observation, it is worth discussing the possible limit of our experimental methodology with regards to spatial resolution. Egerton described<sup>52</sup> the delocalization of an excitation with a parameter  $d_{50}$  such that 50% of the excitation events occur within a diameter  $d_{50}$ :

$$d_{50} \sim 0.8\lambda \left[ \frac{E_0}{E} \right]^{3/4} \quad (1)$$

Here  $E_0$  is the energy of the primary electrons,  $E$  the energy at which the excitation occurs, and  $\lambda$  the wavelength of the

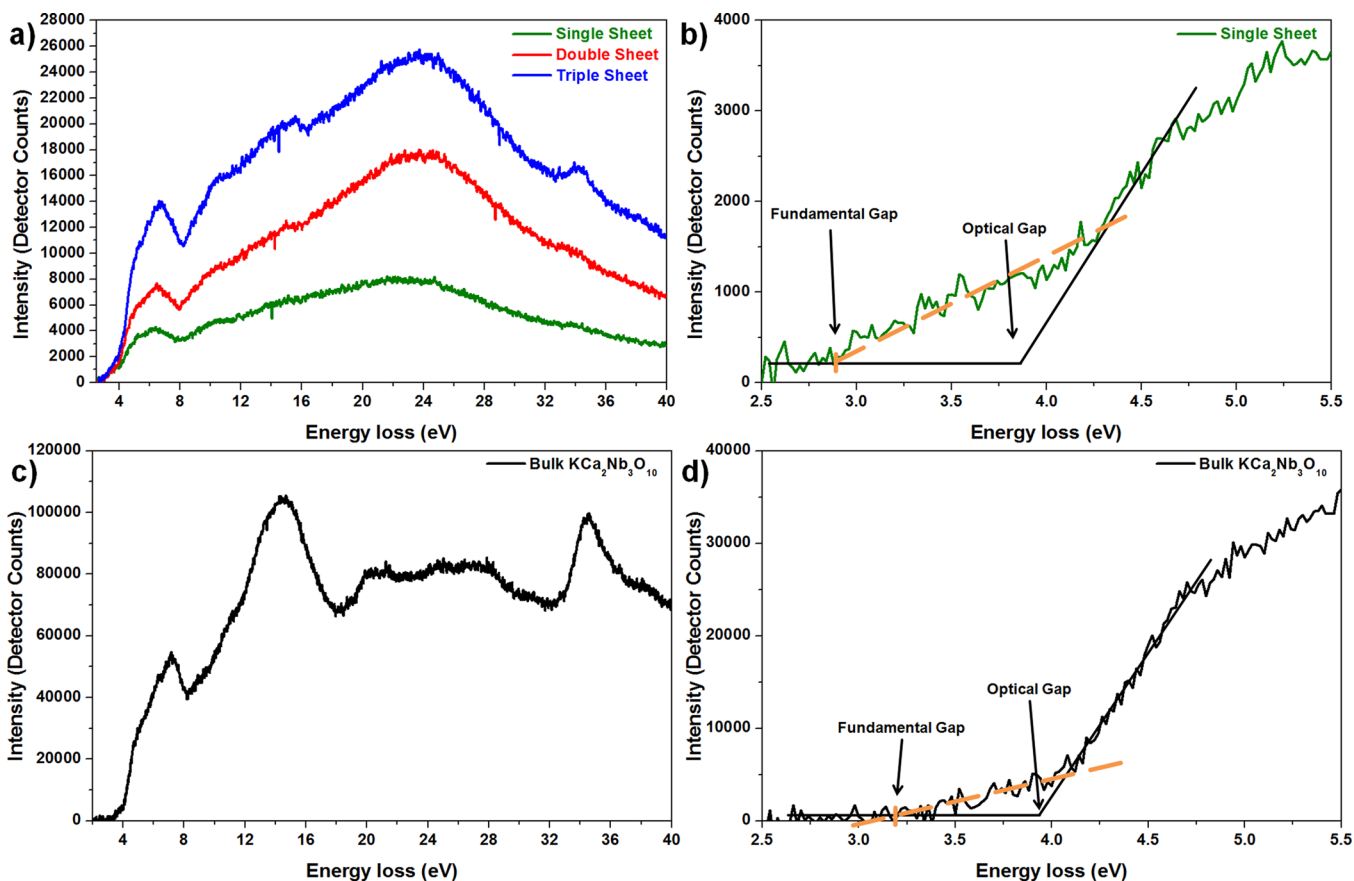


**Figure 8.** VEEL spectra after ZLP subtraction, acquired from single, double, and triple sheet regions (a). The close-up of the spectrum taken from the single sheet (b) indicates a fundamental gap at  $2.9 \pm 0.2$  eV and a monotonic increase in the scattering cross section. The optical gap is located at  $3.8 \pm 0.2$  eV. The VEEL spectrum (c) of the bulk  $\text{KCa}_2\text{Nb}_3\text{O}_{10}$  after ZLP subtraction<sup>32</sup> shows clear similarities with that of the nanosheets, especially for the single electron valence excitations, while the plasmon region differs strongly. The zoom-in (d) was used to determine the fundamental and the optical gap.

**Table 1. Fundamental and Optical Band Gap Values Determined via VEELS and UV–Vis Diffuse Reflectance Data Using the Tauc Plot Method**

	fundamental gap (eV)		optical gap (eV)	
	sheet	bulk	sheet	bulk
VEELS	$2.9 \pm 0.2$	$3.2 \pm 0.1$	$3.8 \pm 0.2$	$3.9 \pm 0.1$
Tauc plot	$3.4 \pm 0.1$	$3.4 \pm 0.1$	$3.6 \pm 0.1$	$3.6 \pm 0.1$

electrons. Using this relation, we determine  $d_{50}$  to be about 9 nm.

Surface plasmons are a collective excitation mode of the electrons at the surface. They can significantly contribute to the scattering cross section in the case of nanostructures, as has been shown previously by Nelayah et al. for the case of Ag nanoprisms.<sup>53</sup> It has been suggested that surface plasmons can interfere with the valence loss excitations, thereby making the extraction of the band gap difficult.<sup>54,55</sup> As such, it is necessary to check the possible implications of surface plasmon excitations to our band gap measurements. Surface plasmons are an important excitation mode when the sample is excited in so-called *aloof* condition; i.e., the beam in STEM mode is placed right outside the edge of the sample.<sup>56</sup> Such *aloof* measurements are often performed for nanostructures.<sup>48,57–60</sup> The viability of this method is based on the fact that the valence loss excitations are delocalized,<sup>48,49</sup> and as such a beam in *aloof* conditions (within a few nanometers from the edge) is able to

trigger low energy valence loss excitations. Despite that, we did not observe a measurable signal above the noise level when we acquired VEEL spectra by placing the beam 1 nm off the sheet. A possible cause for this could be the  $[\text{TBA}]^+$  ligands which screen the electric field and hinder its effective penetration into the  $[\text{Ca}_2\text{Nb}_3\text{O}_{10}]^-$  layer. Determining the exact cause of the limited scattering cross section in *aloof* mode excitation for our nanosheets is beyond the scope of the present study and as such was not further investigated.

Cerenkov losses have also been reported<sup>54</sup> to be another hindrance to band gap measurements using VEELS; however, they become dominant only in thicker samples (thickness greater than 0.6 times the mean free path length) or for very small collection angles (few  $\mu\text{rad}$ ).<sup>25</sup> Given that our measurements were done on regions only a few nanometers thick using a collection angle of 9.5 mrad, the possibility of strong contributions due to Cerenkov radiation interfering in our measurements can be neglected.

The structural similarity between the  $[\text{TBA}_x\text{H}_{1-x}]^+[\text{Ca}_2\text{Nb}_3\text{O}_{10}]^-$  nanosheets and  $\text{KCa}_2\text{Nb}_3\text{O}_{10}$  makes it worth comparing the electronic structure between the two materials. Our DFT calculations<sup>32</sup> using the Tran–Blaha modified Becke–Johnson potential (which predict band gaps with high accuracy<sup>61</sup>) suggest a fundamental band gap of 3.1 eV for  $\text{KCa}_2\text{Nb}_3\text{O}_{10}$  whereby the partial density of states contribution of K atoms to the valence and conduction bands adjacent to the band gap is negligible. The calculated

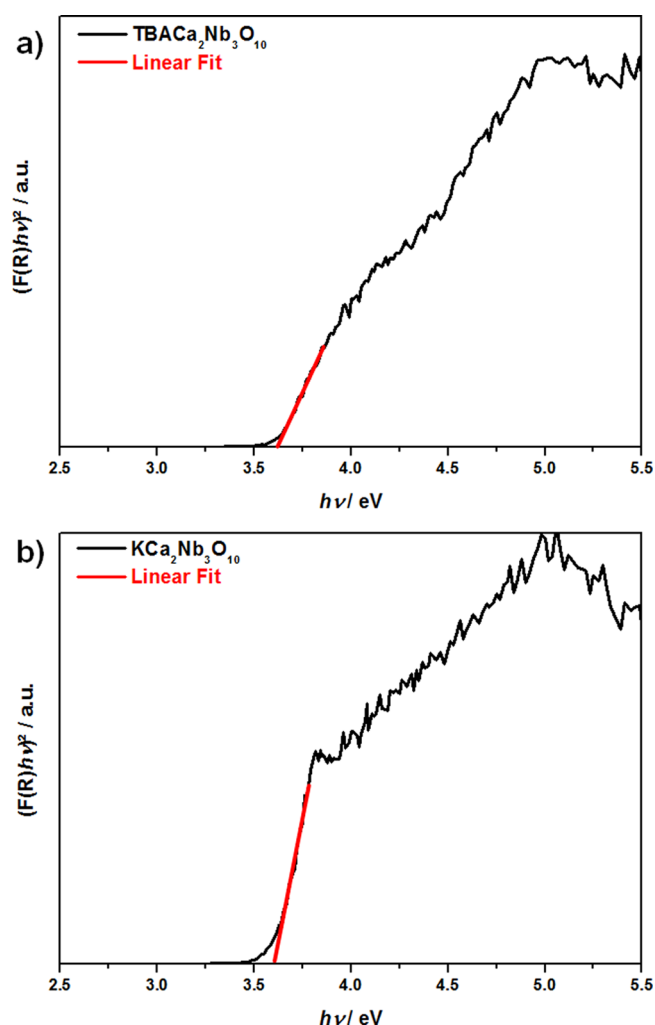


**Figure 9.** Tauc plots determined from UV–vis reflectance data for (a) dried restacked  $[\text{TBA}_x\text{H}_{1-x}]^+[\text{Ca}_2\text{Nb}_3\text{O}_{10}]^-$  nanosheets and (b)  $\text{KCa}_2\text{Nb}_3\text{O}_{10}$  bulk. Assuming a direct semiconductor,  $(F(R)h\nu)^2$  was plotted against the photon energy. A linear extrapolation was used to determine the optical band gap, which is  $3.6 \pm 0.1$  eV for both materials. The fundamental gap is located around  $3.4 \pm 0.1$  eV.

fundamental gap value is in good agreement with the one obtained by VEELS measurements for bulk  $\text{KCa}_2\text{Nb}_3\text{O}_{10}$ , which is  $3.2 \pm 0.1$  eV.<sup>32</sup> This indicates that removal of the K atoms during exfoliation does not change the fundamental band gap value significantly when considering the experimental error ( $2.9 \pm 0.2$  eV for the nanosheet versus  $3.2 \pm 0.1$  eV for the bulk).

The  $\text{Ca-M}_{2,3}$  edge at 34 eV<sup>44</sup> (representing the excitation of Ca 3p electrons into unoccupied levels) can be hardly identified in the VEEL spectra acquired from the single sheet (Figure 8a). In spectra acquired from the triple sheet region, the  $\text{Ca-M}_{2,3}$  edge becomes more pronounced, and in the spectra acquired from the bulk  $\text{KCa}_2\text{Nb}_3\text{O}_{10}$  it becomes very intense (Figure 8c). Furthermore, one sees an increase in the intensity of the plasmon excitation which is expected on the basis of increase in the thickness as one moves from regions of single to double to triple sheet. The most distinguishable difference between the VEELS from nanosheets and the bulk material is the region between 18 and 30 eV. In the  $[\text{TBA}_x\text{H}_{1-x}]^+[\text{Ca}_2\text{Nb}_3\text{O}_{10}]^-$  nanosheets we observe a broad plasmon in this energy range, which has a greater scattering cross section than that for single

electron excitations. Given the structural similarity between the nanosheet and the bulk materials, the difference in VEELS in this energy loss regime would imply that the plasmon excitation in the nanosheets is predominantly contributed or modified by the ligand layer.

## SUMMARY AND CONCLUSION

We have successfully demonstrated the use of STEM-VEELS for determining the band gap of  $[\text{TBA}_x\text{H}_{1-x}]^+[\text{Ca}_2\text{Nb}_3\text{O}_{10}]^-$  nanosheets with a high spatial resolution. These sheets are highly crystalline and have minimal interaction between the individual nanosheets when they stack on each other. The measured fundamental and optical band gap values of individual sheets are close to the band gap values of the bulk  $\text{KCa}_2\text{Nb}_3\text{O}_{10}$  phase and considered invariant within the range of experimental error. This is in accordance with UV–vis reflectance data and might be also valid for other 2D materials obtained via intercalation–exfoliation from anisotropic bulk oxide phases. The measured band gap values provide insight into the electronic structure at high spatial resolution of about 9 nm. The sheets disintegrate within 5 s under the electron beam bombardment; therefore, to effectively determine the band gap fast acquisition is paramount. The valence electron excitations in the nanosheet are similar to that in the bulk  $\text{KCa}_2\text{Nb}_3\text{O}_{10}$  except for the strong plasmon excitation, most likely caused by the ligand layer.

In summary, STEM-VEELS presents a powerful tool for the extraction of local band gaps and as such will be a suitable method for a wide variety of nanostructures which are inaccessible to alternative techniques with typically low spatial resolution. The technique is able to probe also wide band gap semiconductors with thicknesses in the range of a few nanometers and without optical signatures in the visible range.

## AUTHOR INFORMATION

### Corresponding Author

\*E-mail [scheu@mpie.de](mailto:scheu@mpie.de); Tel +49 (0)211 67 92 720 (C.S.).

### Author Contributions

K.S.V., Y.K., and C.Z. contributed equally.

### Notes

The authors declare no competing financial interest.

## ACKNOWLEDGMENTS

This work was partially supported by the German Science Foundation (DFG) through the cluster of excellence Nano-systems Initiative Munich (NIM) and the Center for Nanoscience (CeNS). K.S.V. is grateful to the Elite Network of Bavaria for financial support. P.B. was supported by the SFB-F41 (ViCoM) project of the Austrian Science Funds (FWF). We thank B. Tuffy and K. Schwinghammer for UV–vis measurements and R. Eicher for CHNS analysis.

## ABBREVIATIONS

HAADF, high angle annular dark field; STEM, scanning transmission electron microscopy; TBA, tetra-*n*-butylammonium; TEM, scanning transmission electron microscopy; VEELS, valence electron energy loss spectroscopy.

## REFERENCES

- (1) Novoselov, K. S.; Geim, A. K.; Morozov, S. V.; Jiang, D.; Katsnelson, M. I.; Grigorieva, I. V.; Dubonos, S. V.; Firsov, A. A. Two-

Dimensional Gas of Massless Dirac Fermions in Graphene. *Nature* **2005**, *438*, 197–200.

(2) Ma, R.; Sasaki, T. Nanosheets of Oxides and Hydroxides: Ultimate 2D Charge-Bearing Functional Crystallites. *Adv. Mater. (Weinheim, Ger.)* **2010**, *22*, 5082–5104.

(3) Coleman, J. N.; Lotya, M.; O'Neill, A.; Bergin, S. D.; King, P. J.; Khan, U.; Young, K.; Gaucher, A.; De, S.; Smith, R. J.; et al. Two-Dimensional Nanosheets Produced by Liquid Exfoliation of Layered Materials. *Science* **2011**, *331*, 568–571.

(4) Novoselov, K. S.; Jiang, D.; Schedin, F.; Booth, T. J.; Khotkevich, V. V.; Morozov, S. V.; Geim, A. K. Two-Dimensional Atomic Crystals. *Proc. Natl. Acad. Sci. U. S. A.* **2005**, *102*, 10451–10453.

(5) Smith, R. J.; King, P. J.; Lotya, M.; Wirtz, C.; Khan, U.; De, S.; O'Neill, A.; Duesberg, G. S.; Grunlan, J. C.; Moriarty, G.; et al. Large-Scale Exfoliation of Inorganic Layered Compounds in Aqueous Surfactant Solutions. *Adv. Mater. (Weinheim, Ger.)* **2011**, *23*, 3944–3948.

(6) Dion, M.; Ganne, M.; Tournoux, M. Nouvelles Familles De Phases  $M^I M^{II}_2 Nb_3 O_{10}$  a Feuilletés "Perovskites. *Mater. Res. Bull.* **1981**, *16*, 1429–1435.

(7) Jacobson, A. J.; Johnson, J. W.; Lewandowski, J. T. Interlayer Chemistry between Thick Transition-Metal Oxide Layers: Synthesis and Intercalation Reactions of  $K[Ca_2 Na_{n-3} Nb_n O_{3n+1}]$ . *Inorg. Chem.* **1985**, *24*, 3727–3729.

(8) Treacy, M. M. J.; Rice, S. B.; Jacobson, A. J.; Lewandowski, J. T. Electron Microscopy Study of Delamination in Dispersions of the Perovskite-Related Layered Phases  $K[Ca_2 Na_{n-3} Nb_n O_{3n+1}]$ : Evidence for Single-Layer Formation. *Chem. Mater.* **1990**, *2*, 279–286.

(9) Schaak, R. E.; Mallouk, T. E. Self-Assembly of Tiled Perovskite Monolayer and Multilayer Thin Films. *Chem. Mater.* **2000**, *12*, 2513–2516.

(10) Li, B.-W.; Osada, M.; Ozawa, T. C.; Ebina, Y.; Akatsuka, K.; Ma, R.; Funakubo, H.; Sasaki, T. Engineered Interfaces of Artificial Perovskite Oxide Superlattices Via Nanosheet Deposition Process. *ACS Nano* **2010**, *4*, 6673–6680.

(11) Compton, O. C.; Carroll, E. C.; Kim, J. Y.; Larsen, D. S.; Osterloh, F. E. Calcium Niobate Semiconductor Nanosheets as Catalysts for Photochemical Hydrogen Evolution from Water. *J. Phys. Chem. C* **2007**, *111*, 14589–14592.

(12) Okamoto, Y.; Ida, S.; Hyodo, J.; Hagiwara, H.; Ishihara, T. Synthesis and Photocatalytic Activity of Rhodium-Doped Calcium Niobate Nanosheets for Hydrogen Production from a Water/Methanol System without Cocatalyst Loading. *J. Am. Chem. Soc.* **2011**, *133*, 18034–18037.

(13) Osada, M.; Sasaki, T. Two-Dimensional Dielectric Nanosheets: Novel Nanoelectronics from Nanocrystal Building Blocks. *Adv. Mater. (Weinheim, Ger.)* **2012**, *24*, 210–228.

(14) Chang, L.; Holmes, M. A.; Waller, M.; Osterloh, F. E.; Moule, A. J. Calcium Niobate Nanosheets as a Novel Electron Transport Material for Solution-Processed Multi-Junction Polymer Solar Cells. *J. Mater. Chem.* **2012**, *22*, 20443–20450.

(15) Ziegler, C.; Werner, S.; Bugnet, M.; Worsching, M.; Duppel, V.; Botton, G. A.; Scheu, C.; Lotsch, B. V. Artificial Solids by Design: Assembly and Electron Microscopy Study of Nanosheet-Derived Heterostructures. *Chem. Mater.* **2013**, *25*, 4892–4900.

(16) Kim, Y.-H.; Kim, H.-J.; Osada, M.; Li, B.-W.; Ebina, Y.; Sasaki, T. 2D Perovskite Nanosheets with Thermally-Stable High-Kappa Response: A New Platform for High-Temperature Capacitors. *ACS Appl. Mater. Interfaces* **2014**, *6*, 19510–19514.

(17) Li, B.-W.; Osada, M.; Ebina, Y.; Akatsuka, K.; Fukuda, K.; Sasaki, T. High Thermal Robustness of Molecularly Thin Perovskite Nanosheets and Implications for Superior Dielectric Properties. *ACS Nano* **2014**, *8*, 5449–5461.

(18) Ebina, Y.; Sasaki, T.; Watanabe, M. Study on Exfoliation of Layered Perovskite-Type Niobates. *Solid State Ionics* **2002**, *151*, 177–182.

(19) Sabio, E. M.; Chi, M.; Browning, N. D.; Osterloh, F. E. Charge Separation in a Niobate Nanosheet Photocatalyst Studied with Photochemical Labeling. *Langmuir* **2010**, *26*, 7254–7261.

(20) Ida, S.; Okamoto, Y.; Koga, S.; Hagiwara, H.; Ishihara, T. Black-Colored Nitrogen-Doped Calcium Niobium Oxide Nanosheets and Their Photocatalytic Properties under Visible Light Irradiation. *RSC Adv.* **2013**, *3*, 11521–11524.

(21) Akatsuka, K.; Takanashi, G.; Ebina, Y.; Haga, M.-A.; Sasaki, T. Electronic Band Structure of Exfoliated Titanium- and/or Niobium-Based Oxide Nanosheets Probed by Electrochemical and Photoelectrochemical Measurements. *J. Phys. Chem. C* **2012**, *116*, 12426–12433.

(22) Domen, K.; Yoshimura, J.; Sekine, T.; Tanaka, A.; Onishi, T. A Novel Series of Photocatalysts with an Ion-Exchangeable Layered Structure of Niobate. *Catal. Lett.* **1990**, *4*, 339–343.

(23) Williams, D. B.; Carter, C. B. *Transmission Electron Microscopy, a Textbook for Materials Science; Part 3: Imaging, Chapter 22*; Springer Science + Business Media: New York, 2009; pp 379–388.

(24) Muller, D. A. Structure and Bonding at the Atomic Scale by Scanning Transmission Electron Microscopy. *Nat. Mater.* **2009**, *8*, 263–270.

(25) Gu, L.; Srot, V.; Sigle, W.; Koch, C.; van Aken, P.; Scholz, F.; Thapa, S. B.; Kirchner, C.; Jetter, M.; Rühle, M. Band-Gap Measurements of Direct and Indirect Semiconductors Using Monochromated Electrons. *Phys. Rev. B: Condens. Matter Mater. Phys.* **2007**, *75*, 195214.

(26) Park, J.; Heo, S.; Chung, J.-G.; Kim, H.; Lee, H.; Kim, K.; Park, G.-S. Bandgap Measurement of Thin Dielectric Films Using Monochromated STEM-EELS. *Ultramicroscopy* **2009**, *109*, 1183–1188.

(27) Kuykendall, T.; Ulrich, P.; Aloni, S.; Yang, P. Complete Composition Tunability of InGaN Nanowires Using a Combinatorial Approach. *Nat. Mater.* **2007**, *6*, 951–956.

(28) Erni, R.; Browning, N. D. Quantification of the Size-Dependent Energy Gap of Individual CdSe Quantum Dots by Valence Electron Energy-Loss Spectroscopy. *Ultramicroscopy* **2007**, *107*, 267–273.

(29) Keller, D.; Buecheler, S.; Reinhard, P.; Pianezzi, F.; Pohl, D.; Surrey, A.; Rellinghaus, B.; Erni, R.; Tiwari, A. N. Local Band Gap Measurements by VEELS of Thin Film Solar Cells. *Microsc. Microanal.* **2014**, *20*, 1246–1253.

(30) Dennenwaldt, T.; Ciston, J.; Dahmen, U.; Ching, W. Y.; Pucher, F. J.; Schnick, W.; Scheu, C. High-Resolution Spectroscopy of Bonding in a Novel  $BeP_2N_4$  Compound. *Microsc. Microanal.* **2014**, *20*, 664–670.

(31) Jiang, N.; Spence, J. C. H. Valence Electron Energy-Loss Spectroscopy Study of  $ZrSiO_4$  and  $ZrO_2$ . *Ultramicroscopy* **2013**, *134*, 68–76.

(32) Virdi, K. S.; Kauffmann, Y.; Ziegler, C.; Ganter, P.; Lotsch, B. V.; Kaplan, W. D.; Blaha, P.; Scheu, C. Electronic Structure of  $KCa_2Nb_3O_{10}$  as Envisaged by Density Functional Theory and Valence Electron Energy Loss Spectroscopy. *Phys. Rev. B: Condens. Matter Mater. Phys.* **2013**, *87*, 115108.

(33) King, P. D. C.; Veal, T. D.; Fuchs, F.; Wang, C. Y.; Payne, D. J.; Bourlange, A.; Zhang, H.; Bell, G. R.; Cimalla, V.; Ambacher, O.; et al. Band Gap, Electronic Structure, and Surface Electron Accumulation of Cubic and Rhombohedral  $In_2O_3$ . *Phys. Rev. B: Condens. Matter Mater. Phys.* **2009**, *79*, 10.

(34) Williams, D. B.; Carter, C. B. *Transmission Electron Microscopy, a Textbook for Materials Science; Part 1: Basics, Chapter 4*; Springer Science + Business Media: New York, 2009; pp 64–68.

(35) Müllejan, H.; French, R. Interband Electronic Structure of a near-Sigma Grain Boundary in Alpha-Alumina Determined by Spatially Resolved Valence Electron Energy-Loss Spectroscopy. *J. Phys. D: Appl. Phys.* **1996**, *29*, 1751–1760.

(36) Chen, Z.; Dinh, H. N.; Miller, E. S. 4 Analysis of Band Gap Energies from Uv-Vis Spectra. In *Photoelectrochemical Water Splitting - Standards, Experimental Methods, and Protocols*; Chen, Z., Dinh, H. N., Miller, E., Eds.; Springer: New York, 2013; pp 57–60.

(37) Tandon, S. P.; Gupta, J. P. Measurement of Forbidden Energy Gap of Semiconductors by Diffuse Reflectance Technique. *Phys. Status Solidi B* **1970**, *38*, 363–367.

- (38) Dresselhaus, M. S. *Solid State Physics Part II Optical Properties of Solids*; Oxford University Press: 2001.
- (39) Wood, D. L.; Tauc, J. Weak Absorption Tails in Amorphous Semiconductors. *Phys. Rev. B* **1972**, *5*, 3144–3151.
- (40) Osada, M.; Sasaki, T. Exfoliated Oxide Nanosheets: New Solution to Nanoelectronics. *J. Mater. Chem.* **2009**, *19*, 2503–2511.
- (41) Song, Y.; Iyi, N.; Hoshida, T.; Ozawa, T. C.; Ebina, Y.; Ma, R.; Miyamoto, N.; Sasaki, T. Accordion-Like Swelling of Layered Perovskite Crystals Via Massive Permeation of Aqueous Solutions into 2D Oxide Galleries. *Chem. Commun.* **2015**, *51*, 17068–17071.
- (42) Tokumitsu, T.; Toda, K.; Aoyagi, T.; Sakuraba, D.; Uematsu, K.; Sato, M. Powder Neutron Diffraction Study of Layered Perovskite,  $\text{KCa}_2\text{Nb}_3\text{O}_{10}$ . *J. Ceram. Soc. Jpn.* **2006**, *114*, 795–797.
- (43) Brydson, R. *Electron Energy Loss Spectroscopy*; Taylor and Francis: Oxon, UK, 2006.
- (44) Ahn, C. C.; Krivanek, O. L.; Burgner, R. P.; Disko, M. M.; Swann, P. R. *EELS Atlas*; HREM Facility, Arizona State University: Tempe, AZ, 1983.
- (45) Bach, D.; Schneider, R.; Gerthsen, D.; Verbeeck, J.; Sigle, W. EELS of Niobium and Stoichiometric Niobium-Oxide Phases—Part I: Plasmon and near-Edges Fine Structure. *Microsc. Microanal.* **2009**, *15*, 505–523.
- (46) Fink, J.; Müller-Heinzerling, T.; Scheerer, B.; Speier, W.; Hillebrecht, F. U.; Fuggle, J. C.; Zaanen, J.; Sawatzky, G. A. 2p Absorption Spectra of the 3d Elements. *Phys. Rev. B: Condens. Matter Mater. Phys.* **1985**, *32*, 4899–4904.
- (47) Wang, J.; Li, Q.; Ronning, C.; Stichtenoth, D.; Müller, S.; Tang, D. Nanomaterial Electronic Structure Investigation by Valence Electron Energy Loss Spectroscopy—an Example of Doped ZnO Nanowires. *Micron* **2008**, *39*, 703–708.
- (48) García de Abajo, F. J. Optical Excitations in Electron Microscopy. *Rev. Mod. Phys.* **2010**, *82*, 209–275.
- (49) Egerton, R. F. *Electron Energy-Loss Spectroscopy in the Electron Microscope*, 3rd ed.; Springer Science + Business Media: New York, 2011.
- (50) Krivanek, O. L.; Disko, M. M.; Taftø, J.; Spence, J. C. H. Electron Energy Loss Spectroscopy as a Probe of the Local Atomic Environment. *Ultramicroscopy* **1982**, *9*, 249–254.
- (51) Couillard, M.; Kociak, M.; Stéphan, O.; Botton, G. A.; Colliex, C. Multiple-Interface Coupling Effects in Local Electron-Energy-Loss Measurements of Band Gap Energies. *Phys. Rev. B: Condens. Matter Mater. Phys.* **2007**, *76*, 165131.
- (52) Egerton, R. F. New Techniques in Electron Energy-Loss Spectroscopy and Energy-Filtered Imaging. *Micron* **2003**, *34*, 127–139.
- (53) Nelayah, J.; Kociak, M.; Stephan, O.; Garcia de Abajo, F. J.; Tence, M.; Henrard, L.; Taverna, D.; Pastoriza-Santos, I.; Liz-Marzan, L. M.; Colliex, C. Mapping Surface Plasmons on a Single Metallic Nanoparticle. *Nat. Phys.* **2007**, *3*, 348–353.
- (54) Stöger-Pollach, M. Optical Properties and Bandgaps from Low Loss EELS: Pitfalls and Solutions. *Micron* **2008**, *39*, 1092–1110.
- (55) Jiang, N.; Spence, J. C. H. Valence Electron Energy-Loss Spectroscopy Study of  $\text{ZrSiO}_4$  and  $\text{ZrO}_2$ . *Ultramicroscopy* **2013**, *134*, 68–76.
- (56) Huang, M. R. S.; Erni, R.; Lin, H.-Y.; Wang, R.-C.; Liu, C.-P. Characterization of Wurtzite ZnO Using Valence Electron Energy Loss Spectroscopy. *Phys. Rev. B: Condens. Matter Mater. Phys.* **2011**, *84*, 155203.
- (57) Arenal, R.; Stéphan, O.; Kociak, M.; Taverna, D.; Loiseau, A.; Colliex, C. Electron Energy Loss Spectroscopy Measurement of the Optical Gaps on Individual Boron Nitride Single-Walled and Multiwalled Nanotubes. *Phys. Rev. Lett.* **2005**, *95*, 127601.
- (58) Walls, M. G.; Howie, A. Dielectric Theory of Localised Valence Energy Loss Spectroscopy. *Ultramicroscopy* **1989**, *28*, 40–42.
- (59) Echenique, P. M.; Howie, A.; Ritchie, R. H. Comment on 'near-Field Electron Energy Loss Spectroscopy of Nanoparticles'. *Phys. Rev. Lett.* **1999**, *83*, 658–658.
- (60) Itskovsky, M. A.; Cohen, H.; Maniv, T. Radiative Interaction of a Focused Relativistic Electron Beam in Energy-Loss Spectroscopy of Nanoscopic Platelets. *Phys. Rev. B: Condens. Matter Mater. Phys.* **2008**, *78*, 045419.
- (61) Tran, F.; Blaha, P. Accurate Band Gaps of Semiconductors and Insulators with a Semilocal Exchange-Correlation Potential. *Phys. Rev. Lett.* **2009**, *102*, 226401.